


Cite this: *RSC Adv.*, 2017, 7, 46263

# Simple synthesis of a double-shell hollow structured $\text{MnO}_2@ \text{TiO}_2$ composite as an anode material for lithium ion batteries†

Yibo Su, Jian Zhang, Kai Liu, Zeya Huang, Xiancang Ren and Chang-An Wang \*

A double-shell hollow structured  $\text{MnO}_2@ \text{TiO}_2$  anode material has been successfully synthesized through a two-step template method. The monodispersed carbon spheres synthesized through a hydrothermal method act as the templates. The inner part of the carbon template acts as a sacrificial template to form the void and the outer part of it plays the role of self-template to synthesize hollow  $\text{MnO}_2$  spheres. The composition, crystallinity, morphology, and valence state of the final product  $\text{MnO}_2@ \text{TiO}_2$  are characterized using X-ray diffraction, scanning electron microscopy, transmission electron microscopy, and X-ray photoelectron spectroscopy. The electrochemical performances of the double-shell hollow structured  $\text{MnO}_2@ \text{TiO}_2$  anode material have been comprehensively improved. The specific capacity of the composite retains  $802 \text{ mA h g}^{-1}$  at the current rate of  $200 \text{ mA g}^{-1}$  after 200 cycles, and it can still retain about  $400 \text{ mA h g}^{-1}$  at a higher current rate of  $1 \text{ A g}^{-1}$ . Finally, a more detailed charging/discharging process of  $\text{MnO}_2$  is proposed.

Received 30th August 2017  
Accepted 25th September 2017  
DOI: 10.1039/c7ra09628c  
[rsc.li/rsc-advances](http://rsc.li/rsc-advances)

## 1. Introduction

Lithium ion batteries have been widely used in portable electronic devices and electric vehicles because of their high energy density as well as long cycle life. Nevertheless, increasing capacity requirements make it necessary to develop new electrode materials, for example anode materials, to substitute current carbonaceous materials that possess a theoretical lithium capacity of  $372 \text{ mA h g}^{-1}$ .<sup>1–3</sup> Transition metal oxides are potential substitutions due to their common high theoretical specific capacity, based on a conversion reaction. One of the most promising candidates,  $\text{MnO}_2$ , has attracted much attention since it was first used as an anode material by Poizot,<sup>4</sup> because of its natural advantages: (1)  $\text{MnO}_2$  has a high theoretical specific capacity of  $1232 \text{ mA h g}^{-1}$ , much higher than that of graphite;<sup>5–7</sup> (2)  $\text{MnO}_2$  displays a moderate discharge voltage plateau of 0.4 V, which is lower than most of transition metal oxides, guaranteeing a high output voltage,<sup>8</sup> and is higher than carbonaceous materials, making the precipitation of lithium metal harder under the circumstances of high current rate or low temperature, and further declare a safer working condition;<sup>10</sup> (3) the natural resource of  $\text{MnO}_2$  is plentiful and its preparation process is mature and diverse.<sup>9–11</sup> However, there are still some severe problems hindering the industrialization

paces of  $\text{MnO}_2$  anode materials in that: (1)  $\text{MnO}_2$  shows a big volume effect during charge/discharge cycles, causing pulverization of itself and even electrode film; (2)  $\text{MnO}_2$  exhibits an extremely low electronic and ionic conductivity, leading to a bad rate capacity; (3)  $\text{MnO}_2$  displays a very low coulombic efficiency during the first cycle.<sup>12,13</sup>

In order to solve these problems, different strategies have been attempted. In the beginning, the attention was focused on diminishing the particle size and making enough void for  $\text{MnO}_2$  to expand. A more elaborate structure could shorten the diffusion path of ions and alleviate the volume expansion. Thus,  $\text{MnO}_2$  nanomaterials with different crystalline phase, morphology and structure were synthesized, such as hollow  $\alpha$ - $\text{MnO}_2$  urchin and nanotubes,<sup>14,15</sup>  $\beta$ - $\text{MnO}_2$  nanorods,<sup>16</sup> nanoporous  $\gamma$ - $\text{MnO}_2$  hollow microspheres and nanocubes.<sup>17</sup> Nevertheless, their cycle performances were still unsatisfied and the rate capacity was even worse as a result of the poor conductivity of  $\text{MnO}_2$ . Therefore, so far, more and more works have been carried out to fabricate the composite materials of  $\text{MnO}_2$  with various conducting materials such as carbonaceous materials,<sup>18–21</sup> organic conducting polymers<sup>22,23</sup> and inorganic semiconductors.<sup>24–26</sup>  $\text{TiO}_2$  is an ideal candidate of inorganic semiconductor for  $\text{MnO}_2$  coating not only because of its contribution to conductivity, but also it has a good structural stability during charge/discharge cycles due to a very small volume expansion. In addition,  $\text{TiO}_2$  is nontoxic, abundant, and not expensive so that it could be used as coating materials in industrial scale.<sup>27–29</sup>

In this paper, a new double-shell hollow structured  $\text{MnO}_2@ \text{TiO}_2$  has been synthesized *via* a two-step template method. The  $\text{TiO}_2$  coating improves the electrochemical performance of  $\text{MnO}_2$

State Key Lab of New Ceramics and Fine Processing, School of Materials Science and Engineering, Tsinghua University, 100084, Beijing, China. E-mail: wangca@mail.tsinghua.edu.cn

† Electronic supplementary information (ESI) available. See DOI: 10.1039/c7ra09628c

and inner void provides a space for the volume effect during charge/discharge cycles. Moreover, this preparation method is a simple and short process, which is more adaptable to an efficient industrial production than all the above-mentioned works.

## 2. Experimental

### 2.1 Material synthesis

All reagents were used without further purification. In a typical procedure to prepare the double-shell hollow structured  $\text{MnO}_2@\text{TiO}_2$  composite, carbon spheres with an average diameter of 200 nm were firstly fabricated through a hydro-thermal method using glucose.<sup>30</sup> 0.15 g as-prepared carbon spheres and 0.3 g  $\text{KMnO}_4$  were separately dispersed in 50 ml and 20 ml distilled water through a 10 min ultrasonic processing, and then the two solutions were mixed together to react for 30 min to get  $\text{C}@\text{MnO}_2$ . Finally, the brown product was filtered and washed with water and ethanol for three times.

The synthesized  $\text{C}@\text{MnO}_2$  and 0.3 ml tetrabutyl titanate (TBOT) were dispersed in 50 ml anhydrous ethanol solution under ultrasonic treatment. 0.3 ml ammonium hydroxide diluted with 1.5 ml anhydrous ethanol was added into the solution dropwise, and the mixed solution reacted under magnetic stirring at 70 °C for 1 h. The precursor  $\text{C}@\text{MnO}_2\text{-TiO}(\text{OH})_2$  was obtained after centrifugal washing with absolute ethanol and drying for 6 h, and was finally annealed at 450 °C for 2 h to get  $\text{MnO}_2@\text{TiO}_2$  with a double-shell structure.

### 2.2 Material characterization

The morphology of the samples was observed with a field-emission scanning electron microscope (FESEM, ZEISS MERLIN Compact, Germany). The structure and the element contents were characterized through TEM and EDS with a transmission electron microscope (TEM, JEOL JEM-2010, Japan). The crystal structure was analyzed by X-ray diffraction (XRD, Bruker D8 ADVANCE, Germany) with  $\text{Cu K}\alpha$  ( $\lambda = 0.154178$  nm) radiation. The diffraction patterns were recorded from 10° to 80° at a scanning rate of 6°  $\text{min}^{-1}$ . The valence state was implied with X-ray photoelectron spectroscopy (XPS) with an ESCALAB 250 Xi electron spectrometer from VG Scientific using 300 W Al  $\text{K}\alpha$  radiation.

### 2.3 Battery assembling and electrochemical measurement

The working electrodes for electrochemical tests were prepared by a conventional procedure. First, 70 wt% of active material was dispersed with 15 wt% of super P and 15 wt% of polyvinylidene fluoride (PVDF) binder adequately in *N*-methyl-2-pyrrolidone (NMP), and the mixture was casted on a copper sheet. Then, after a drying and pressing process at 5 MPa, the electrode film was cut into several discs with a diameter of 12.5 mm. The average loading of active material was around 1 mg. At last, the LIR2032 coin cells were assembled in an Ar-filled glove box (Mikrouna (Super1220/750/900), China) by using the as-prepared electrodes as the working electrode, lithium foils as the counter and reference electrode, Celgard 2325 as the separator, and 1 M LiPF<sub>6</sub> in EC : DEC (1 : 1 by volume) as the

electrolyte. The charge/discharge test was performed using a land cell test system (Land CT2001A, China) at various current rates between 0.01 V and 3.0 V (vs.  $\text{Li/Li}^+$ ) at ambient. Cyclic voltammetry (CV) was performed using an electrochemical workstation (CHI600E, China) between 0.01 V and 3.0 V at a sweep rate of 0.2  $\text{mV s}^{-1}$ . The electrochemical impedance spectra (EIS) of the cells was also measured on the electrochemical workstation over a frequency range from 10<sup>5</sup> Hz to 0.1 Hz with an amplitude of 5  $\text{mV}_{\text{rms}}$ .

## 3. Results and discussion

Double-shell structured  $\text{MnO}_2@\text{TiO}_2$  composite and porous  $\text{MnO}_2$  were successfully achieved by a carbon-template method, as shown in Fig. 1. First, according to the previous work in our group,<sup>31</sup> the core-shell structured  $\text{C}@\text{MnO}_2$  could be easily fabricated through the reaction in ambient between carbon spheres and  $\text{KMnO}_4$  with appropriate concentration in a short time. To certify the existing of carbon core, the  $\text{C}@\text{MnO}_2$  was calcined at 350 °C for 1 h, and the TEM images of the samples were shown in Fig. S1.† Considering the fact that the temperature range of decomposition of carbon spheres is 300–500 °C, which is denoted in Fig. S2,† the small void in Fig. S1(b)† arises clearly as a result of the oxidative decomposition of the carbon core. Then, some of the  $\text{C}@\text{MnO}_2$  samples were treated with TBOT to coat  $\text{TiO}(\text{OH})_2$  outside the  $\text{C}@\text{MnO}_2$  spheres and finally calcined at 450 °C for 2 h to prepare  $\text{MnO}_2@\text{TiO}_2$  composite, while the others were directly heated to 450 °C for 2 h to fabricate porous  $\text{MnO}_2$ , which is depicted by TEM in Fig. S1(c and d).† It is notable that the porous  $\text{MnO}_2$  possesses an interesting sphere structure constructed by crossing crystalline  $\text{MnO}_2$  nanorods. For convenience, the  $\text{C}@\text{MnO}_2$ ,  $\text{MnO}_2@\text{TiO}_2$  and the porous  $\text{MnO}_2$  are named as CM, MT-450 and M-450, respectively.

Fig. 2 shows X-ray diffraction (XRD) patterns of as-prepared  $\text{C}@\text{MnO}_2$ , MT-450 and M-450. Although the XRD pattern of CM displays poor crystallinity, it could still be indexed as  $\delta$ -phase  $\text{MnO}_2$  (JCPDS no. 80-1098), similar to the previous reports.<sup>32</sup> There are the same diffraction peaks for MT-450 and M-450 appearing at  $2\theta = 28.8$ , 37.5 and 60.3°, which can be ascribed to the (310), (211) and (521) reflections of  $\alpha$ - $\text{MnO}_2$  (PDF-44-0141), respectively. The diffraction peaks of  $\text{TiO}_2$  in MT-

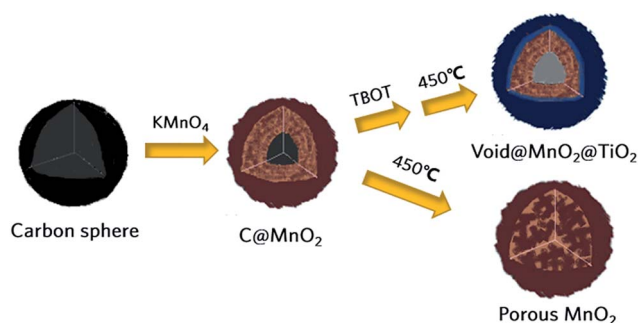


Fig. 1 Schematic synthetic route for double shell structured  $\text{MnO}_2@\text{TiO}_2$  composite and porous  $\text{MnO}_2$  in contrast.



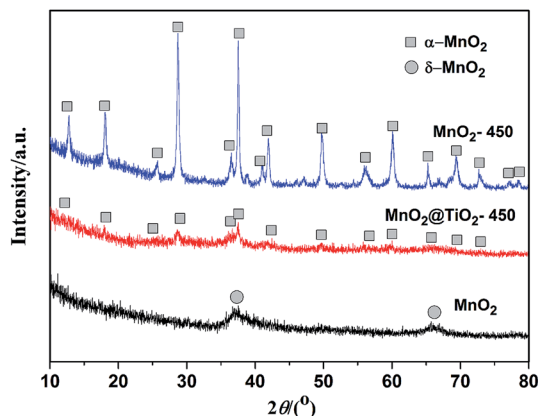


Fig. 2 The XRD patterns of as-prepared  $C@MnO_2$ ,  $MnO_2@TiO_2$ -450 and  $MnO_2$ -450.

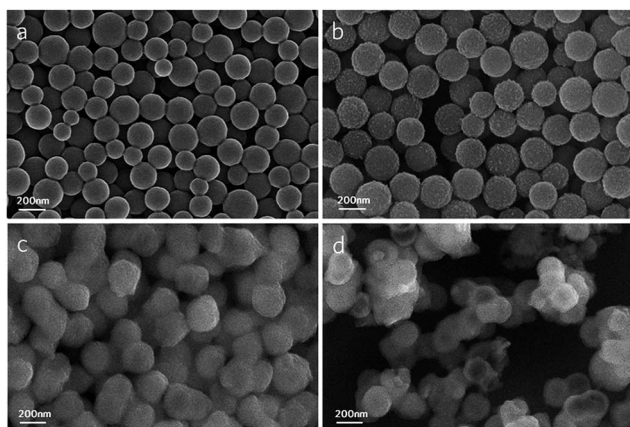


Fig. 3 SEM images of carbon spheres (a),  $C@MnO_2$  (b),  $C@MnO_2@TiO(OH)_2$  (c),  $MnO_2@TiO_2$  (d).

450 are so weak because of the very thin shell covered on the surface of  $MnO_2$ . It is worth noticing that MT-450 exhibits worse crystallinity than M-450, which demonstrates the resistant effect of  $TiO_2$  for the crystalline process of  $MnO_2$ . A relatively worse crystallinity contributes to a higher first-cycle coulombic efficiency, because the insertion reaction of  $MnO_2$  at a relatively high voltage ( $>2$  V) is nearly irreversible,<sup>9,33</sup> which will be further discussed below.

Field-emission scanning electron microscope (FESEM) was used to characterize the morphology of all the typical samples in each of the steps, as can be seen in Fig. 3. And the four images are all photographed at the same magnification. The carbon spheres in Fig. 3a have a good monodispersity and an average diameter of 150–200 nm. Comparatively, the average diameter of  $C@MnO_2$  in Fig. 3b is a little bigger than carbon spheres as a result of the Kirkendall effect, based on which Li<sup>31</sup> set forth a “surface-softening” diffusion model to illustrate the whole process in detail. Under the treatment of  $KMnO_4$ , the long tangled chains of aromatic nuclei with reactive oxygen functional groups decomposes into short carbon chains, which is capable of diffusing through the  $MnO_2$  layer and maintains reducibility at the same time. In other words, the short carbon chains in carbon spheres diffuse outward, meanwhile the  $KMnO_4$  diffuses inward and react with short carbon chains to form  $MnO_2$  outside the spheres causing a relatively bigger diameter. After coating with  $TiO(OH)_2$ , voids appear in some of the spheres in Fig. 3c due to good solubility of short carbon chains in anhydrous ethanol. In the process of aging at 70 °C, short carbon chains in some spheres tend to dissolve out into the anhydrous ethanol, thus form the voids. In addition, there are some solid spheres without voids, probably because the  $TiO(OH)_2$  shell is dense enough to prevent short carbon chains from dissolving out. Finally after calcination, the spheres in goal product MT-450 (Fig. 3d) are almost all hollow spheres.

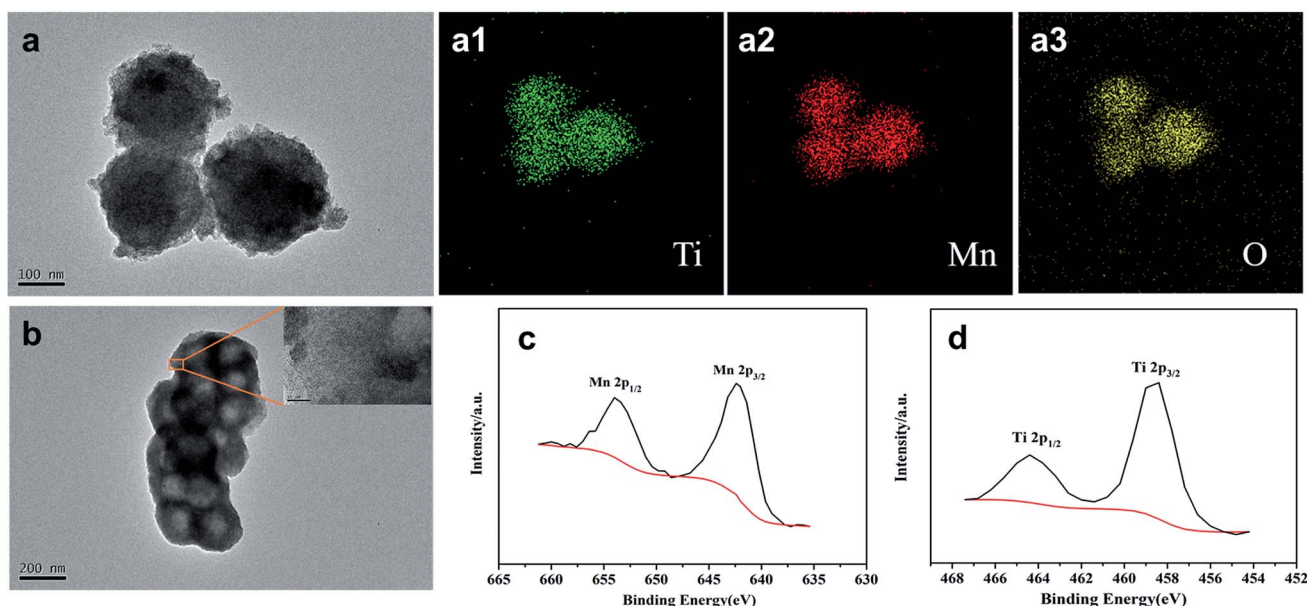


Fig. 4 TEM images of  $C@MnO_2@TiO(OH)_2$  (a) and  $MnO_2@TiO_2$  (b), the small image inside (b) is the high-resolution TEM image of the marked zone; EDS-Mappings of  $C@MnO_2@TiO(OH)_2$  (a1: titanium, a2: manganese, a3: oxygen); XPS images of  $MnO_2@TiO_2$  (c: Ti 2p, d: Mn 2p).





To further verify the components and structure of the resulting product MT-450, transmission electron microscope (TEM) and X-ray photoelectron spectroscopy (XPS) tests were carried out as shown in Fig. 4. According to Fig. 4a (containing 4a1–4a3), the  $\text{C@MnO}_2\text{@TiO(OH)}_2$  precursor spheres partly consist of Mn, Ti and O atoms, announcing a successful coating of  $\text{TiO(OH)}_2$ . From Fig. 4b, it is clearly to see the hollow structure of the goal product MT-450 as well as the amorphous  $\text{TiO}_2$  in the high-resolution TEM image, which is the magnification of the marked zone in Fig. 4b. EDS has also been conducted to certify the component of MT-450, which could be found in

Fig. S3.† The chemical composition of MT-450 was deeply characterized by using XPS, as illustrated in Fig. 4(c and d). The peaks at 642.3 eV, 654.0 eV, 458.5 eV and 464.3 eV are assigned to Mn 2p<sub>3/2</sub>, Mn 2p<sub>1/2</sub>, Ti 2p<sub>3/2</sub> and Ti 2p<sub>1/2</sub>, respectively, indicating that Mn and Ti exist in MK-450 mainly in the form of  $\text{Mn}^{4+}$  and  $\text{Ti}^{4+}$ , which agrees with the reported values.<sup>34–37</sup>

MT-450 is compared with M-450 (and M-350, discussed in Fig. S4†) in terms of cycling performance, electrochemical impedance and rate capacity, tested in coin cells with lithium foil as the reference and counter electrode. The obtained results are presented in Fig. 5. According to Fig. 5a, MT-450 displays

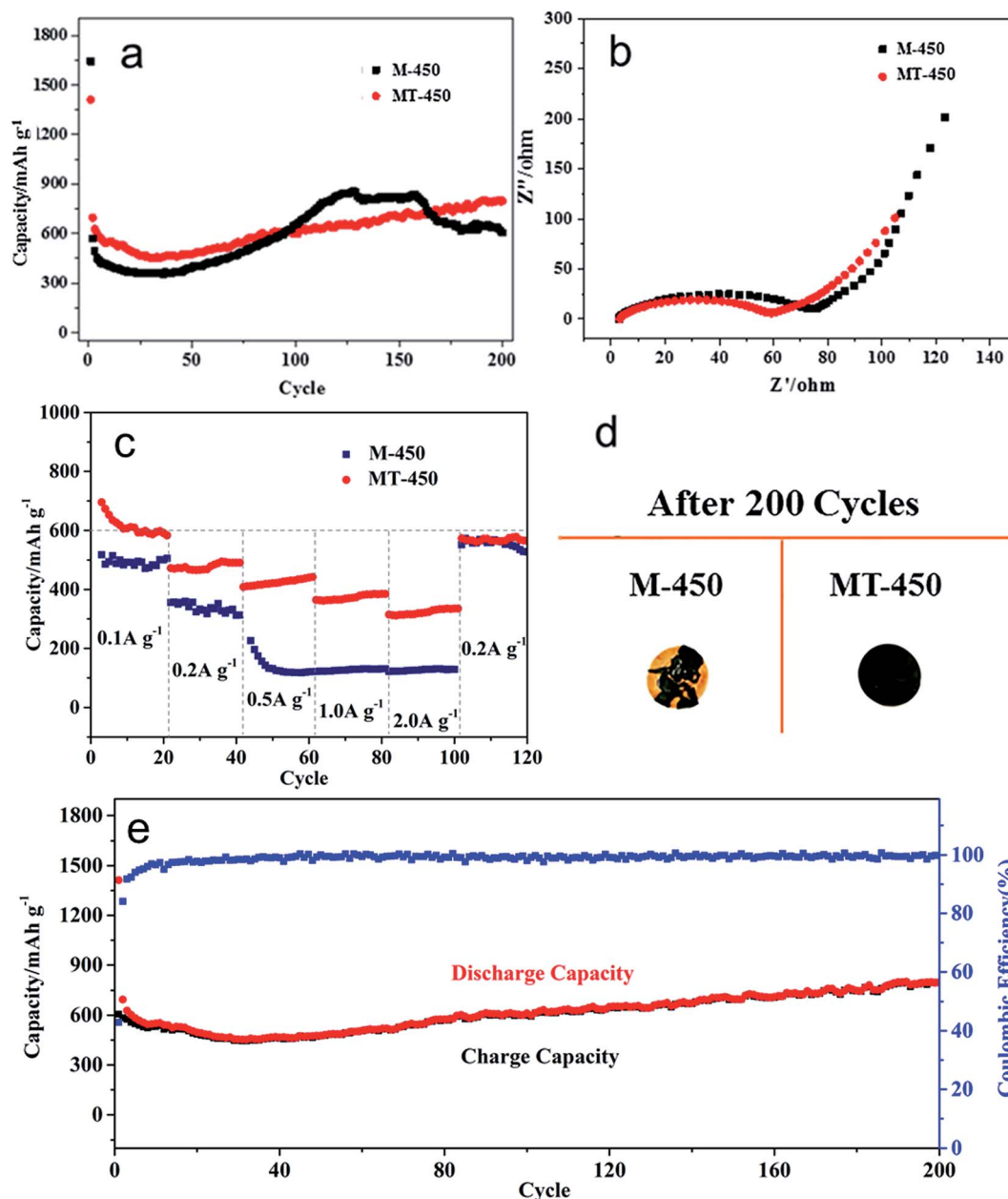


Fig. 5 (a) The comparison of cycling performance of MT-450 and M-450 in the range of 0.01–3 V vs.  $\text{Li}^+/\text{Li}$  at a current rate of  $200 \text{ mA g}^{-1}$  in 200 cycles; (b) electrochemical impedance spectra of MT-450 and M-450; (c) variation of the specific capacity with cycling at different current densities, and (d) the anode sheet appearance of M-450 and MT-450 after 200 cycles; (e) the cyclability of the MT-450 at a current rate of  $200 \text{ mA g}^{-1}$  within 200 cycles.



a better specific capacity retention of 802 mA h g<sup>-1</sup> (comparing to M-450 of 605 mA h g<sup>-1</sup>) after 200 cycles at a current rate of 200 mA h g<sup>-1</sup>. This improvement could be attributed to the protection of TiO<sub>2</sub>, which avoids direct contact between MnO<sub>2</sub> and electrolyte, thus alleviating side reactions and volume effect during cycles. The tendency of capacity decrease before the first 30 cycles suggesting that fresh SEI keeps generating until the 30<sup>th</sup> cycle.<sup>36</sup> As for the notable rising of specific capacity, it is common for MnO<sub>x</sub> anode materials,<sup>29</sup> which is attributed to an activation process of the active materials.<sup>38</sup>

Fig. 5b presents similar electrochemical impedance spectra (EIS) of M-450 and MT-450. The semicircle at high frequencies of MT-450 is relatively smaller, which implies a lower charge transfer resistance ( $R_{ct}$ ) between materials and the electrolyte. That is to say, the coating of TiO<sub>2</sub> promotes the charge transfer of MnO<sub>2</sub> and would further improve its rate capacity. The slope of the straight line at low frequencies of the two samples are nearly the same, which reflecting the same diffusion of lithium ions in the electrolyte.<sup>36</sup> Fig. 5c shows the rate capacity of the two samples at different current densities of 0.1 A g<sup>-1</sup>, 0.2 A g<sup>-1</sup>, 0.5 A g<sup>-1</sup>, 1 A g<sup>-1</sup> and 2 A g<sup>-1</sup> within 120 cycles. The two samples have similar behaviors when the current rate is lower or equal to 0.2 A g<sup>-1</sup>. While, once the current rate rises to 0.5 A g<sup>-1</sup> or bigger, its specific capacity declines sharply to an extremely low value of about 130 mA h g<sup>-1</sup>. Comparatively, the MT-450 still presents a specific capacity of around 450 mA h g<sup>-1</sup> and 400 mA h g<sup>-1</sup> respectively at the current rate of 0.5 A g<sup>-1</sup> and

1 A g<sup>-1</sup>, even with more than 300 mA h g<sup>-1</sup> left at 2 A g<sup>-1</sup>, which proves that the coating of TiO<sub>2</sub> does contribute to its rate capacity. Without the protection of TiO<sub>2</sub>, at last, powdering and stripping of the active material of M-450, as photographed in Fig. 5d, leads to a rapid capacity fading. Fig. 5e shows the good cyclability of the MT-450 at a current rate of 200 mA g<sup>-1</sup> within 200 cycles, accompanied by an average coulombic efficiency of more than 99%.

From the cyclic voltammograms (CV) of MT-450 and M-450 in different cycles, shown in Fig. 6, it can be clearly seen that a new pair of charge/discharge peaks emerges at about 1 V and 2.1 V after 200 cycles. According to the reported work, there exists two charging/discharging process for MnO<sub>x</sub> anode materials.<sup>39,40</sup> However, as far as we know, there is little work have been reported demonstrating the mechanism of the two charging/discharging process of MnO<sub>2</sub>. Herein, it is going to be further discussed.

In this work, the MnO<sub>2</sub> nanospheres are crystallized as  $\alpha$ -MnO<sub>2</sub>, as shown in Fig. 2. At the beginning of discharging process, lithium ions insert into the tunnels of  $\alpha$ -MnO<sub>2</sub> without affecting its structure. Then, with inserted lithium ions increasing and the voltage lowering down, the Mn and O atoms get reorganized and gradually resulting in more stabilized Li<sub>x</sub>-MnO<sub>2</sub> structures with defect rock salt character until the voltage is lower than 0.5 V.<sup>9</sup> After that, the new coming Li would replace Mn through a reduction reaction, forming Mn and Li<sub>2</sub>O. The reactions are:

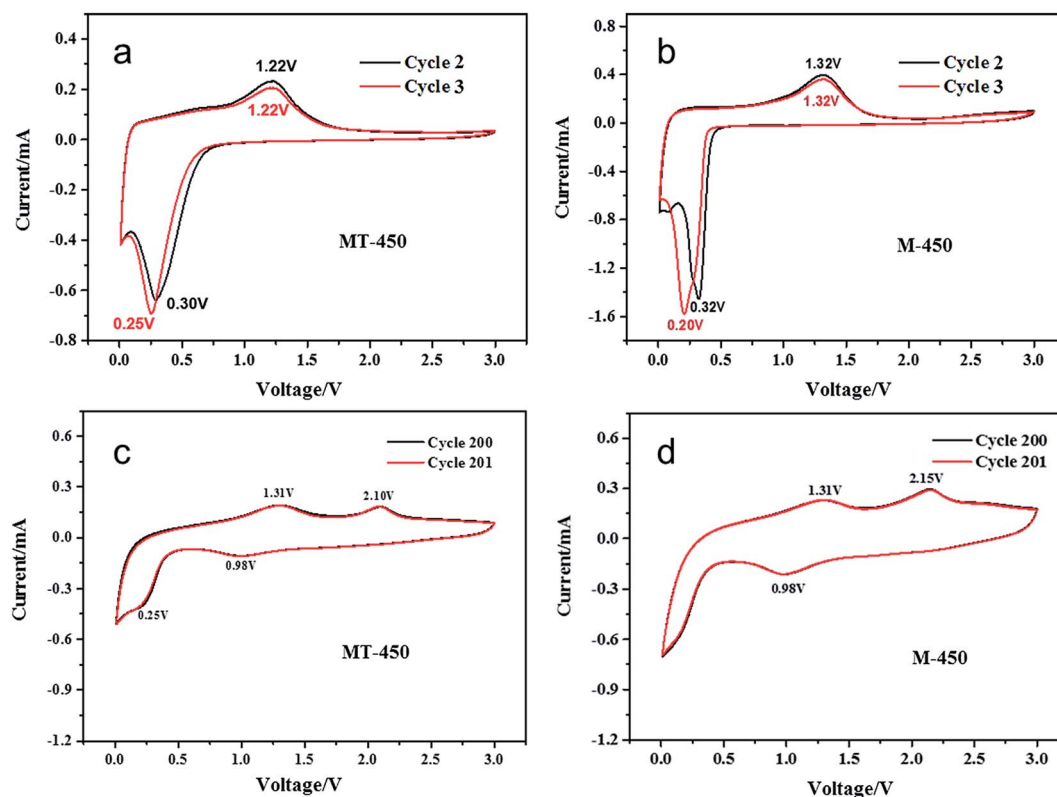
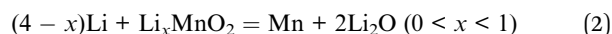


Fig. 6 Cyclic voltammograms at a scan rate of 0.2 mV s<sup>-1</sup> in the range of 0.01–3 V of MT-450 and M-450 in cycle 2–3 (a, b) and cycle 200–201 (c, d).





During charging, the process is reversed. However, for  $\text{Li}_x\text{-MnO}_2$ , it is hard to extract all of its  $\text{Li}^+$  because it's more stable to keep a rock salt structure. The reactions are written as follows.



Further, for the next discharging process, because of the incompleteness of lithium extraction for  $\text{Li}_x\text{MnO}_2$ , the high-voltage discharging reaction is adapted to:



Apparently, the capacity of this part is determined by process (4), and it could contribute a capacity proportion of less than 25%, which is corresponding to the valence change from  $\text{Mn}^{4+}$  to  $\text{Mn}^{3+}$ . There exists different mechanism of lithium insertion in different range of voltage, therefore, the discharge capacity should be divided into two parts by the threshold of voltage platform, named part A and B in this work as illustrated in Fig. 7. After 200 cycles, part 200-A and 200-B in Fig. 7 are corresponding to process (5) and (2), respectively.

The charge/discharge curves of cycle 1, 10, 50, 100 and 200 of the two samples are put together for comparison, as shown in Fig. 7(a) and (b). From the curves of cycle 1, the discharge capacity corresponding to the voltage range from 3 V to 2 V could be read as  $47 \text{ mA h g}^{-1}$  (a) and  $75 \text{ mA h g}^{-1}$  (b), respectively. This part of discharge capacity is useless and even harmful for the anode material because of its high voltage platform as well as its poor reversibility, leading to a lower first coulombic efficiency. Comparatively, the MT-450 realizes a smaller discharge capacity of  $47 \text{ mA h g}^{-1}$  owing to a worse crystallinity than M-450, and further attains to a higher first coulombic efficiency.

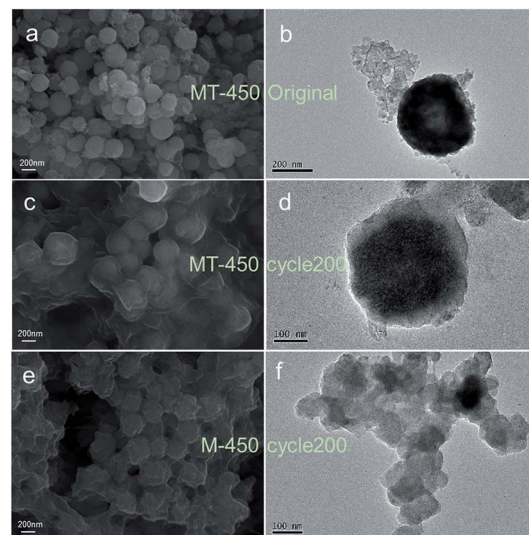


Fig. 8 SEM images and TEM images of original state (a, b) and the 200<sup>th</sup> cycle state (c, d) of the MT-450 and the state of M-450 after 200 cycles (e, f) on copper foil. The component of (d) is certified with EDS, whose results is seen in Fig. S5†

After 200 cycles, many of the active materials of M-450 collapse completely with massive SEI, while MT-450 displays an eminent structural stability, as shown in Fig. 8. Because  $\text{MnO}_2$  is well confined in the  $\text{TiO}_2$  shell in MT-450 (verified in Fig. S5†).  $\text{MnO}_2$  can only expand inwards in the process of lithium insertion. The inner  $\text{MnO}_2$  hollow spheres end up into porous spheres, which is also an eligible structure for a superior anode material. Based on the above characterizations, a schematic of morphological evolution process of MT-450 and M-450 during cycling is illustrated in Fig. 9. The structure of MT-450 will switch from double-shell hollow structure to porous core-shell structure and maintain stable in hundreds of cycles. Without protective  $\text{TiO}_2$  shell,  $\text{MnO}_2$  will end up with pieces of fragments wearing an increasing thickness of SEI during cycles. From Fig. S5,† we can find that the atom percent ratio of Mn : Ti is about 5 : 1. So, the content of  $\text{TiO}_2$  is calculated as around

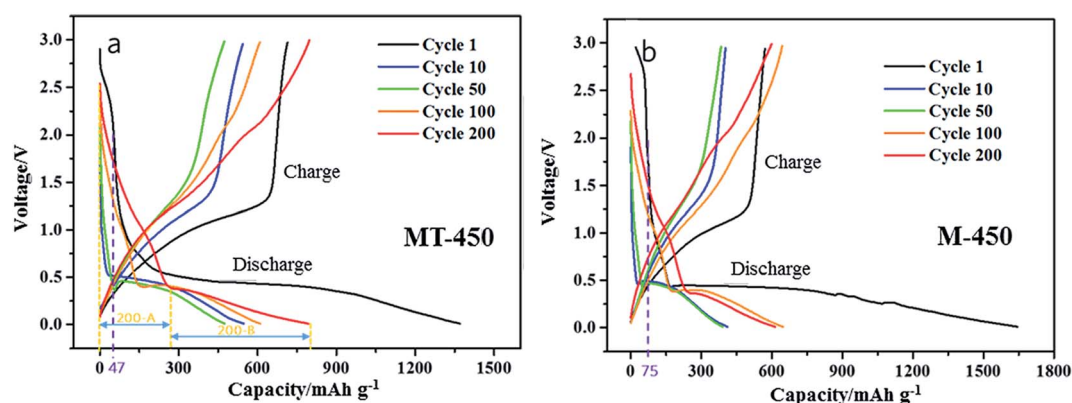


Fig. 7 The charge/discharge voltage profiles in the range of 0.01–3 V at a current rate of  $200 \text{ mA h g}^{-1}$  of MT-450 and M-450 (a, b). In a typical cycle (for example, cycle 200), the discharge capacity can be divided into two parts by the by the threshold of its voltage platform, as is depicted in (a). The first part of capacity is named "A", and the second part "B".



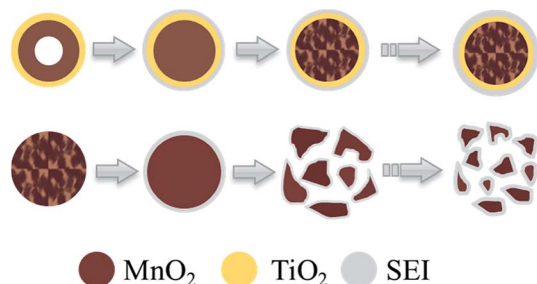


Fig. 9 Schematic of morphological evolution process of MT-450 and M-450 during cycling.

15.5 wt%. The content of  $\text{TiO}_2$  have to be moderate because a high  $\text{TiO}_2$  contents will cause a capacity decrease owing to the low theoretical specific capacity of  $\text{TiO}_2$  ( $335 \text{ mA h g}^{-1}$ , far less than that of  $\text{MnO}_2$  with  $1232 \text{ mA h g}^{-1}$ ), while a low  $\text{TiO}_2$  contents will result in an incomplete coating, which will greatly discount the protection effect of  $\text{TiO}_2$ .

## 4. Conclusions

The double-shell structured  $\text{MnO}_2@/\text{TiO}_2$  anode material has been successfully synthesized through a simple two-step template method. The outer part of carbon template spheres reacts with  $\text{KMnO}_4$  to form “hollow”  $\text{MnO}_2$ , and then, after a  $\text{TiO}_2$  coating, the inner part is moved out by calcination to form “void”, making the  $\text{MnO}_2$  truly hollow. In the  $\text{MnO}_2@/\text{TiO}_2$  composite, both of  $\text{MnO}_2$  and  $\text{TiO}_2$  display poor crystallinity.  $\text{TiO}_2$  shell could improve the electrochemical performances of  $\text{MnO}_2@/\text{TiO}_2$  in the following four aspects: (1)  $\text{TiO}_2$  shell hinders the crystalline process of  $\text{MnO}_2$ , leading to a worse crystallinity than pure  $\text{MnO}_2$  at the same temperature, which is beneficial to a higher first-cycle coulombic efficiency. (2)  $\text{TiO}_2$  shell protects  $\text{MnO}_2$  from contacting electrolyte directly, and avoids unnecessary loss of active material to form solid-electrolyte interface (SEI). (3)  $\text{TiO}_2$  shell confines  $\text{MnO}_2$  and compels it to expand only inwards to avoid volume effect during cycles. (4)  $\text{TiO}_2$  shell enhances the conductivity of  $\text{MnO}_2$  to further improve its rate capacity. At last, a more detailed charging/discharging process of  $\text{MnO}_2$  is firstly put forward.

## Conflicts of interest

There are no conflicts to declare.

## Acknowledgements

The authors would like to acknowledge the grants from the National Natural Science Foundation of China (NSFC-No. 51572145).

## References

- 1 B. Xu, C. R. Fell, M. F. Chi and Y. S. Meng, Identifying surface structural changes in layered Li-excess nickel manganese

oxides in high voltage lithium ion batteries: A joint experimental and theoretical study, *Energy Environ. Sci.*, 2011, **4**, 2223–2233.

- 2 Y. M. Sun, H. W. Lee, Z. W. Seh, N. Liu, J. Sun, Y. Z. Li and Y. Cui, High-capacity battery cathode prelithiation to offset initial lithium loss, *Nat. Energy*, 2016, **1**, 1–7.
- 3 W. M. Zhang, X. L. Wu, J. S. Hu, Y. G. Guo and L. J. Wan, Carbon coated  $\text{Fe}_3\text{O}_4$  nanospindles as a superior anode material for Lithium-Ion batteries, *Adv. Funct. Mater.*, 2008, **18**, 3941–3946.
- 4 P. Poizot, S. Laruelle, S. Grugeon, L. Dupontand and J. M. Tarascon, Nano-sized transition-metal oxides as negative-electrode materials for lithium-ion batteries, *Nature*, 2000, **407**, 496–499.
- 5 A. L. M. Reddy, M. M. Shaijumon, S. R. Gowda and P. M. Ajayan, Coaxial  $\text{MnO}_2$ /Carbon Nanotube Array Electrodes for High-Performance Lithium Batteries, *Nano Lett.*, 2009, **9**, 1002–1006.
- 6 C. X. Guo, M. Wang, T. Chen, X. W. Lou and C. M. Li, A Hierarchically Nanostructured Composite of  $\text{MnO}_2$ /Conjugated Polymer/Graphene for High-Performance Lithium Ion Batteries, *Adv. Energy Mater.*, 2011, **1**, 736–741.
- 7 Y. Wang, Z. J. Han, S. F. Yu, R. R. Song, H. H. Song, K. (Ken) Ostrikov and H. Y. Yang, Core-leaf onion-like carbon/ $\text{MnO}_2$  hybrid nano-urchins for rechargeable lithium-ion batteries, *Carbon*, 2013, **64**, 230–236.
- 8 J. Cabana, L. Monconduit, D. Larcher and M. R. Palacín, Beyond Intercalation- Based Li-Ion Batteries: The State of the Art and Challenges of Electrode Materials Reacting Through Conversion Reactions, *Adv. Mater.*, 2010, **22**, 170–192.
- 9 M. M. Thackeray, Manganese Oxides for Lithium Batteries, *Prog. Solid State Chem.*, 1997, **25**, 1–71.
- 10 J. J. Zhang and A. S. Yu, Nanostructured transition metal oxides as advanced anodes for lithium-ion batteries, *Sci. Bull.*, 2015, **60**, 823–838.
- 11 W. H. Ryu, D. W. Han, W. K. Kim and H. S. Kwon, Facile route to control the surface morphologies of 3D hierarchical  $\text{MnO}_2$  and its Al self-doping phenomenon, *J. Nanopart. Res.*, 2013, **13**, 4777–4784.
- 12 Y. F. Deng, L. N. Wan, Y. Xie, X. S. Qin and G. H. Chen, Recent advances in Mn-based oxides as anode materials for lithium ion batteries, *RSC Adv.*, 2014, **4**, 23914–23935.
- 13 A. L. M. Reddy, M. M. Shaijumon, S. R. Gowda and P. M. Ajayan, Coaxial  $\text{MnO}_2$ /Carbon Nanotube Array Electrodes for High-Performance Lithium Batteries, *Nano Lett.*, 2009, **9**, 1002–1006.
- 14 B. Li, G. Rong, Y. Xie, L. Huang and C. Feng, Low-Temperature Synthesis of  $\alpha\text{-MnO}_2$  Hollow Urchins and Their Application in Rechargeable  $\text{Li}^+$  Batteries, *Inorg. Chem.*, 2006, **45**, 6404–6410.
- 15 L. H. Li, C. Y. Nan, J. Lu, Q. Peng and Y. D. Li,  $\alpha\text{-MnO}_2$  nanotubes: high surface area and enhanced lithium battery properties, *Chem. Commun.*, 2012, **48**, 6945–6947.
- 16 X. P. Fang, X. Lu, X. W. Guo, Y. Mao, Y. S. Hu, J. Z. Wang, Z. X. Wang, F. Wu, H. K. Liu and L. Q. Chen, Electrode





- reactions of manganese oxides for secondary lithium batteries, *Electrochem. Commun.*, 2010, **12**, 1520–1523.
- 17 J. Zhao, Z. Tao, J. Liang and J. Chen, Facile Synthesis of Nanoporous  $\gamma$ -MnO<sub>2</sub> Structures and Their Application in Rechargeable Li-Ion Batteries, *Cryst. Growth Des.*, 2008, **8**, 2799–2805.
  - 18 H. Xia, M. Lai and L. Lu, Nanoflaky MnO<sub>2</sub>/carbon nanotube nanocomposites as anode materials for lithium-ion batteries, *J. Mater. Chem.*, 2010, **20**, 6896–6902.
  - 19 A. P. Yu, H. W. Park, A. Davies, D. C. Higgins, Z. W. Chen and X. C. Xiao, Free-Standing Layer-By-Layer Hybrid Thin Film of Graphene-MnO<sub>2</sub> Nanotube as Anode for Lithium Ion Batteries, *J. Phys. Chem. Lett.*, 2011, **2**, 1855–1860.
  - 20 Y. Zhang, H. Liu, Z. H. Zhu, K. W. Wong, R. Mi, J. Mei and W. M. Lau, A green hydrothermal approach for the preparation of graphene/ $\alpha$ -MnO<sub>2</sub> 3D network as anode for lithium ion battery, *Electrochim. Acta*, 2013, **108**, 465–471.
  - 21 Y. Y. Li, Q. W. Zhang, J. L. Zhu, X. L. Wei and P. K. Shen, An extremely stable MnO<sub>2</sub> anode incorporated with 3D porous graphene-like networks for lithium-ion batteries, *J. Mater. Chem. A*, 2014, **2**, 3163–3168.
  - 22 J. X. Li, M. Z. Zou, Y. Zhao, Y. B. Lin, H. Lai, L. H. Guan and Z. G. Huang, Coaxial MWNTs@MnO<sub>2</sub> confined in conducting PPy for kinetically efficient and long-term lithium ion storage, *Electrochim. Acta*, 2013, **111**, 165–171.
  - 23 M. S. Wu, P. C. J. Chiang, J. T. W. Xiao, J. S. Chen, Q. Lu and X. W. Lou, Porous Spheres Assembled from Polythiophene (PTh)-Coated Ultrathin MnO<sub>2</sub> Nanosheets with Enhanced Lithium Storage Capabilities, *J. Phys. Chem. C*, 2010, **114**, 12048–12051.
  - 24 L. L. Xing, B. He, Y. X. Nie, P. Deng, C. X. Cui and X. Y. Xue, SnO<sub>2</sub>-MnO<sub>2</sub>-SnO<sub>2</sub> sandwich-structured nanotubes as high-performance anodes of lithium ion battery, *Mater. Lett.*, 2013, **105**, 169–172.
  - 25 Q. Wang, D. A. Zhang, Q. Wang, J. Sun, L. L. Xing and X. Y. Xue, High electrochemical performances of  $\alpha$ -MoO<sub>3</sub>@MnO<sub>2</sub> core-shell nanorods as lithium-ion battery anodes, *Electrochim. Acta*, 2014, **146**, 411–418.
  - 26 J. Y. Liao, D. Higgins, G. Lui, V. Chabot, X. C. Xiao and Z. W. Chen, Multifunctional TiO<sub>2</sub>-C/MnO<sub>2</sub> Core-Double-Shell Nanowire Arrays as High-Performance 3D Electrodes for Lithium Ion Batteries, *Nano Lett.*, 2013, **13**, 5467–5473.
  - 27 D. A. Zhang, Q. Wang, Q. Wang, J. Sun, L. L. Xing and X. Y. Xue, Core-shell SnO<sub>2</sub>@TiO<sub>2</sub>-B nanowires as the anode of lithium ion battery with high capacity and rate capability, *Mater. Lett.*, 2014, **128**, 295–298.
  - 28 J. Jin, S. Z. Huang, J. Liu, Y. Li, D. S. Chen, H. E. Wang, Y. Yu, L. H. Chen and B. L. Su, Design of new anode materials based on hierarchical, three dimensional ordered macro-mesoporous TiO<sub>2</sub> for high performance lithium ion batteries, *J. Mater. Chem. A*, 2014, **2**, 9699–9708.
  - 29 D. Wua, R. Yang, Q. X. Sun, L. She, W. X. Jia, R. She, M. Jiang, W. P. Ding and L. M. Peng, Simple Synthesis of TiO<sub>2</sub>/MnO<sub>x</sub> Composite with Enhanced Performances as Anode Materials for Li-Ion Battery, *Electrochim. Acta*, 2016, **211**, 832–841.
  - 30 X. M. Sun and Y. D. Li, Colloidal Carbon Spheres and Their Core/Shell Structures with Noble-Metal Nanoparticles, *Angew. Chem., Int. Ed.*, 2004, **43**, 597–601.
  - 31 S. Li and C. A. Wang, Design and synthesis of hierarchically porous MnO<sub>2</sub>/carbon hybrids for high performance electrochemical capacitors, *J. Colloid Interface Sci.*, 2015, **438**, 61–67.
  - 32 P. Ragupathy, D. H. Park, G. Campet, H. N. Vasan, S. J. Hwang, J. H. Choy and N. Munichandraiah, Remarkable Capacity Retention of Nanostructured Manganese Oxide upon Cycling as an Electrode Material for Supercapacitor, *J. Phys. Chem. C*, 2009, **113**, 6303–6309.
  - 33 V. Pralong, Lithium intercalation into transition metal oxides: A route to generate new ordered rock salt type structure, *Prog. Solid State Chem.*, 2009, **37**, 262–277.
  - 34 X. F. Xie and L. Gao, Characterization of a manganese dioxide/carbon nanotube composite fabricated using an in situ coating method, *Carbon*, 2007, **45**, 2365–2373.
  - 35 Z. C. Yang, C. H. Tang, H. Gong, X. Li and J. Wang, Hollow spheres of nanocarbon and their manganese dioxide hybrids derived from soft template for supercapacitor application, *J. Power Sources*, 2013, **240**, 713–720.
  - 36 X. Q. Chen, H. B. Lin, X. W. Zheng, X. Cai, P. Xia, Y. M. Zhu, X. P. Li and W. S. Li, Fabrication of core-shell porous nanocubic Mn<sub>2</sub>O<sub>3</sub>@TiO<sub>2</sub> as a high-performance anode for lithium ion batteries, *J. Mater. Chem. A*, 2015, **3**, 18198–18206.
  - 37 R. Wang, N. Sakai, A. Fujishima, T. Watanabe and K. Hashimoto, Studies of Surface Wettability Conversion on TiO<sub>2</sub> Single-Crystal Surfaces, *J. Phys. Chem. B*, 1999, **103**, 2188–2194.
  - 38 J. Yue, X. Gu, L. Chen, N. N. Wang, X. L. Jiang, H. Y. Xu, J. Yang and Y. T. Qian, General synthesis of hollow MnO<sub>2</sub>, Mn<sub>3</sub>O<sub>4</sub> and MnO nanospheres as superior anode materials for lithium ion batteries, *J. Mater. Chem. A*, 2014, **2**, 17421–17426.
  - 39 B. Liu, D. Li, Z. J. Liu, L. L. Gu, W. H. Xie, Q. Li, P. Q. Guo, D. Q. Liu and D. Y. He, Carbon-wrapped MnO nanodendrites interspersed on reduced graphene oxide sheets as anode materials for lithium-ion batteries, *Appl. Surf. Sci.*, 2017, **394**, 1–8.
  - 40 M. Kundu, C. C. A. Ng, D. Y. Petrovykh and L. F. Liu, Nickel foam supported mesoporous MnO<sub>2</sub> nanosheet arrays with superior lithium storage performance, *Chem. Commun.*, 2013, **49**, 8459–8461.

